High-Frequency Planetary Waves in the Polar Middle Atmosphere as Seen in a Data Assimilation System

L. COY

E. O. Hulburt Center for Space Research, Naval Research Laboratory, Washington, D.C.

I. ŠTAJNER, A. M. DASILVA, J. JOINER, R. B. ROOD, S. PAWSON, AND S. J. LIN

NASA Goddard Space Flight Center, Greenbelt, Maryland

(Manuscript received 29 January 2003, in final form 18 July 2003)

ABSTRACT

The 4-day wave often dominates the large-scale wind, temperature, and constituent variability in the high-latitude Southern Hemisphere winter near the stratopause. This study examines the winter Southern Hemisphere vortex of 1998 using 4-times-daily output from a data assimilation system to focus on the polar 2-day, wavenumber-2 component of the 4-day wave. The data assimilation system products are from a test version of the finite volume data assimilation system (fvDAS) being developed at the Goddard Space Flight Center (GSFC) and include an ozone assimilation system. Results show that the polar 2-day wave in temperature and ozone dominates over other planetary-scale disturbances during July 1998 at 70°S. The period of the quasi-2-day wave is somewhat shorter than 2 days (about 1.7 days) during July 1998 with an average perturbation temperature amplitude for the month of over 2.5 K. The 2-day wave propagates more slowly than the zonal mean zonal wind, consistent with Rossby wave theory, and has Eliassen–Palm (EP) flux divergence regions associated with regions of negative horizontal potential vorticity gradients, as expected from linear instability theory. Results for the assimilation-produced ozone mixing ratio show that the 2-day wave represents a major source of ozone variation in this region. The ozone wave in the assimilation system is in good agreement with the wave seen in the Polar Ozone and Aerosol Measurement (POAM) ozone observations for the same time period. Some differences from linear instability theory are noted, as well as spectral peaks in the ozone field, not seen in the temperature field, that may be a consequence of advection.

1. Introduction

The 4-day wave is a relatively common planetary-scale stratopause disturbance found mainly during the Southern Hemisphere winter. This high-latitude wave consists of wavenumber-1 (wave 1) and wavenumber-2 (wave 2) (and some higher wavenumber) components moving at nearly the same rotational period (the time for a crest to travel around a latitude circle), about 3–4 days, so that the period of the wave-2 component is about 1.5–2 days. Many studies of the 4-day wave have focused on the wave-1 component because only daily analyses are needed to resolve the period accurately. However, modern data assimilation systems that include the stratosphere often output 4 times a day and so can be used to examine the higher-frequency wave-2 component of the 4-day wave. This paper presents results of the 4-day wave seen in the temperature and ozone fields produced by a global data assimilation system during a time when the wavenumber-2 component was dominant.

The 4-day wave has been described by Venne and Stanford (1979, 1982), Prata (1984), Lait and Stanford (1988), Randel and Lait (1991), Manney (1991), Lawrence et al. (1995), and Lawrence and Randel (1996); more references can be found in Allen et al. (1997). Most of these studies examined satellite radiances, though Manney (1991) used daily analyses provided by the National Centers for Environmental Prediction (NCEP), that combined data assimilation products in the troposphere (at and below 100 hPa) with objective analysis products in the stratosphere (above 100 hPa). The wave originates near the stratopause at the level of the stratospheric jet maximum where the latitudial mean zonal wind shears tend to be largest. The wave is believed to be generated by barotropic and baroclinic instability, the relative importance of either process depending on the particular zonal mean wind configuration. The wave is of interest because it is often the dominant large-scale dynamical feature in the high-latitude Southern Hemisphere winter near the stratopause, perturbing temperatures, constituents, and winds.

Corresponding author address: Lawrence Coy, E. O. Hulburt Center for Space Research, Naval Research Laboratory, Code 7646, 4555 Overlook Avenue SW, Washington, DC 20375-5320.
E-mail: coy@uap2.nrl.navy.mil

The linear barotropic instability problem at the stratopause germane to 4-day wave genesis was first investigated by Hartmann (1983) for idealized latitudinal zonal wind profiles. Hartmann (1983) found that instabilities could occur on both the poleward and equatorward side of jets corresponding to negative zonal mean potential vorticity gradients on both sides of the jet. The zonal phase speeds of the unstable waves were nearly equal to the mean zonal wind speed where $\overline{q}_y$ (the zonal mean potential vorticity gradient) changed sign. This gives shorter rotational periods on the poleward side of the jet (~4 days) and longer rotational periods on the equatorward side of the jet (~15 days) because of the change in length of latitude circles around the globe, even though the phase speeds could be similar on both sides of the jet. Using a quasigeostrophic model, Hartmann (1983) also found that baroclinic effects tended to stabilize and reduce growth rates by confining the vertical extent of the region of strong latitudinal wind shear. In Hartmann (1983) both wavenumbers 1 and 2 had similar growth rates; however, another barotropic model study (Manney et al. 1988) showed that wave 2 became the more unstable mode (rather than wave 1) as the jet became more sharply peaked. Manney et al. (1988) also showed that the waves became more dispersive (i.e., the rotational period had more variation for different wavenumbers) as the jet moved equatorward.

Manney and Randel (1993) used a linear quasigeostrophic model to examine unstable modes in climatological zonal mean winds, including both barotropic and baroclinic effects. They showed that both effects were necessary for realistic growth rates to occur in the zonal mean winds they studied. These results agreed with observational studies (Randel and Lait 1991) that showed strong vertical Eliassen–Palm (EP) fluxes (a baroclinic signature) in some 4-day wave observations. More recent work by Allen et al. (1997) highlighted the general structure of the 4-day wave in terms of the temperatures, winds, and heights associated with a potential vorticity (PV) anomaly.

Stratospheric constituents can respond to the 4-day wave as tracers if they have mean gradients in the wave region and relatively long chemical lifetimes. Using high-latitude middle-atmosphere observations from the *Upper Atmosphere Research Satellite* (*UARS*) Allen et al. (1997) showed a 4-day signal in ozone, while Manney et al. (1998) showed a 4-day signal in water vapor and methane. Both studies modeled the tracers differently. Allen et al. (1997) calculated the linear ozone response to the observed temperature and geostrophic meridional wind signal coupled with simple photochemistry to examine the vertical structure of the ozone signal. Manney et al. (1998) used an isentropic transport model to examine tracer transport associated with the 4-day wave. Both studies showed that the 4-day wave, when active, can explain a large amount of the tracer variability near the polar stratopause.

This paper reports on the higher-frequency, wave-2 component of the 4-day wave using 6-hourly output from a data assimilation system that includes output from an offline ozone assimilation, as well as the standard assimilation-produced mass and wind fields. Following a brief description of the assimilation products and analysis methods (section 2), the assimilation-based 4-day wave diagnostics are presented (section 3). In addition to the ozone assimilation, the 4-day wave can be seen in Polar Ozone and Aerosol Measurement (POAM) observations (section 4). Discussion and conclusions follow in sections 5 and 6, respectively.

2. Analysis

This study uses assimilated products produced by the National Aeronautics and Space Administration's (NASA) Data Assimilation Office (DAO), including output from a meteorological data assimilation system (DAS) and an offline ozone data assimilation system (O3DAS). The analysis in this study was performed using 6-hourly output from both of these assimilated datasets for 1998. These assimilation products provide globally gridded fields of temperature, winds, and ozone, at regular time intervals, by incorporating observations into a general circulation model. The advantages of using assimilated datasets over raw observations for this study include a global grid, better vertical resolution than unprocessed radiance measurements, and dynamically consistent winds and temperatures, suitable for calculating higher-order dynamical quatities.

Meteorological analyses are from a prototype version of NASA's Goddard Earth Observing System version 4 (GEOS-4) DAS, which is referred to as the finite-volume DAS (fvDAS). The same dataset was used by Douglass et al. (2003) and Schoeberl et al. (2003) in studies of transport, mainly in the lower stratosphere. The fvDAS uses the Physical-Space Statistical Analysis Scheme (PSAS; Cohn et al. 1998) and a state-of-the-art general circulation model, the fvGCM. The fvGCM is based on the flux-form semi-Lagrangian dynamical core of Lin and Rood (1996, 1997) and Lin (1997), coupled to the Community Climate Model version 3 (CCM) physics of Kiehl et al. (1988). The model includes a hybrid sigma-pressure vertical coordinate with 55 levels, the upper boundary being at 0.01 hPa. Even though the model extends well into the mesosphere, the meteorological dataset from the fvDAS has no data constraints at pressures lower than 0.4 hPa. This dataset is thus useful for studies from the surface to the lower mesosphere.

The data constraint at the levels of interest for this study comes from the Television Infrared Observation Satellite (TIROS) Operational Vertical Sounder (TOVS) radiances, assimilated in a one-dimensional variational (1DVAR) procedure described by Joiner and Rokke (2000). Until July 1998, data from the National Oceanic

and Atmospheric Administration's *NOAA-11* and *NOAA-14* TOVS were assimilated. TOVS consists of the High Resolution Infrared Sounder (HIRS), a 20-channel IR filter-wheel radiometer; a stratospheric sounding unit (SSU), a three-channel radiometer that uses a pressure-modulation technique; and a microwave sounding unit (MSU), a four-channel microwave radiometer. The channels affecting the upper stratosphere are the two highest peaking SSU channels and HIRS channel 1. To avoid intersatellite biases (upper-stratospheric channels are not bias corrected), the *NOAA-11* SSU channels were not assimilated. After 1 July 1998, data from the *NOAA-15* Advanced TOVS (ATOVS) were added to the assimilation, where the 15-channel Advanced Microwave Sounding Unit (AMSU) replaced the SSU and MSU of previous NOAA satellites. To avoid intersatellite bias between the *NOAA-15* ATOVS and the *NOAA-14* SSU, the *NOAA-14* SSU channels were not assimilated after 1 July 1998.

Meteorological output fields from the fvDAS were used to drive the transport model in the DAO's O3DAS (Štajner et al. 2001). This offline assimilation uses total column ozone from the Total Ozone Mapping Spectrometer (TOMS) instrument in conjunction with coarse profile information from the Solar Backscattered Ultraviolet (SBUV) instrument. The assimilation is performed on a vertical grid with 29 levels spanning the surface to 0.2 hPa, with 9 levels in the troposphere and 20 levels in the stratosphere. Note that the fvGCM used a zonally averaged ozone climatology for its radiative heating calculations, not the three-dimensional ozone assimilation that was run offline. Thus, there is no feedback between the ozone and dynamics.

Both the fvDAS and O3DAS were run, for this study, with a horizontal resolution of 2° latitude × 2.5° longitude. For the analysis performed here, data were interpolated to 36 pressure levels spanning 1000 to 0.2 hPa. Zonal and meridional winds, temperature, and geopotential height from the fvDAS were analyzed alongside the ozone.

A standard Fourier transform package was used on two-dimensional longitude by time arrays to extract the eastward-propagating wave components of interest at a given latitude and height. The Fourier analysis was performed monthly (120–124 points in time). The westward-propagating modes consist mainly of solar tidal periods and are not shown here. Though some higher-wavenumber components also show the 4-day wave, only the dominant wave-1 and wave-2 components are presented here. Eliassen–Palm fluxes and associated heat and momentum fluxes were calculated for a given wavenumber and frequency from the zonal wind, meridional wind, and temperature Fourier coefficients along with the zonally and monthly averaged zonal winds and temperatures. The EP flux formulas were evaluated using spherical, log-pressure coordinates [see Andrews et al. 1987, Eq. (3.5.3a,b), p. 128].

Since plots of EP flux and EP flux divergence will be presented in section 3, a brief review of pertinent equations based on Andrews et al. (1987, sections 3.5 and 3.6) is given here. The EP flux divergence represents the wave forcing of the zonal mean zonal wind in the transformed Eulerian-mean zonal momentum equation [Andrews et al. 1987, Eq. (3.5.2a), p. 128]. The EP flux divergence is also a term in a wave conservation equation:

$$\frac{\partial A}{\partial t} + \nabla \cdot \mathbf{F} = D + O(\alpha^3), \tag{1}$$

[Andrews et al. 1987, Eq. (3.6.2), p. 131], where A is the wave-activity density, D depends on frictional and diabatic effects, and $O(\alpha^3)$ represents nonlinear wave effects. As pointed out in Andrews et al. (1987), A and D depend in a complicated way on particle displacements. This limits the usefulness of Eq. (1) in general; however, a time average of Eq. (1) shows that the time-averaged EP flux divergence pattern must be balanced by the time average of the frictional, diabatic, and nonlinear terms.

The quasigeostropic beta-plane version of Eq. (1) is given by

$$\frac{\partial}{\partial t}\left(\frac{1}{2}\frac{\rho_0\overline{q'^2}}{\overline{q}_y}\right) + \nabla \cdot \mathbf{F} = \frac{\rho_0\overline{Z'q'}}{\overline{q}_y} + O(\alpha^3), \tag{2}$$

[Andrews et al. 1987, Eq. (3.6.5), p. 132], where q is the quasigeostrophic potential vorticity, and Z contains both frictional and diabatic terms. The EP flux divergence, $\nabla \cdot \mathbf{F}$, is now the quasigeostropic EP flux divergence on the beta plane. The prime denotes the deviation from zonal average. Equation (2) can be used to relate the EP flux divergence to linear instability studies, where the right-hand side is neglected so that, for growing wave modes, $\nabla \cdot \mathbf{F}$ will be positive (divergent) in regions of negative $\overline{q}_y$ and negative (convergent) in regions of positive $\overline{q}_y$.

3. Results

The 4-day wave can be seen in the gridded assimilation products. Figure 1 shows longitude time sections for temperature and ozone mixing ratio at 70°S and 2 hPa for July 1998. Both fields show wavenumber-2 features propagating eastward with periods of about 2 days. The peak-to-peak amplitude is on the order of 10 K for temperature and 1 ppmv for ozone. A comparison with independent POAM ozone observations will be given later.

Figure 2 gives a representitive mid-July 2-hPa synoptic view of the South Pole where the wave-2 structure can be seen. The temperature field (Fig. 2a) shows two warm regions with a cold, elongated region in between, located over the pole. Both of these warm regions are also seen in the Met Office stratospheric assimilation (not shown) so the warm regions are unlikely to be a DAO system artifact. However, there are differences in

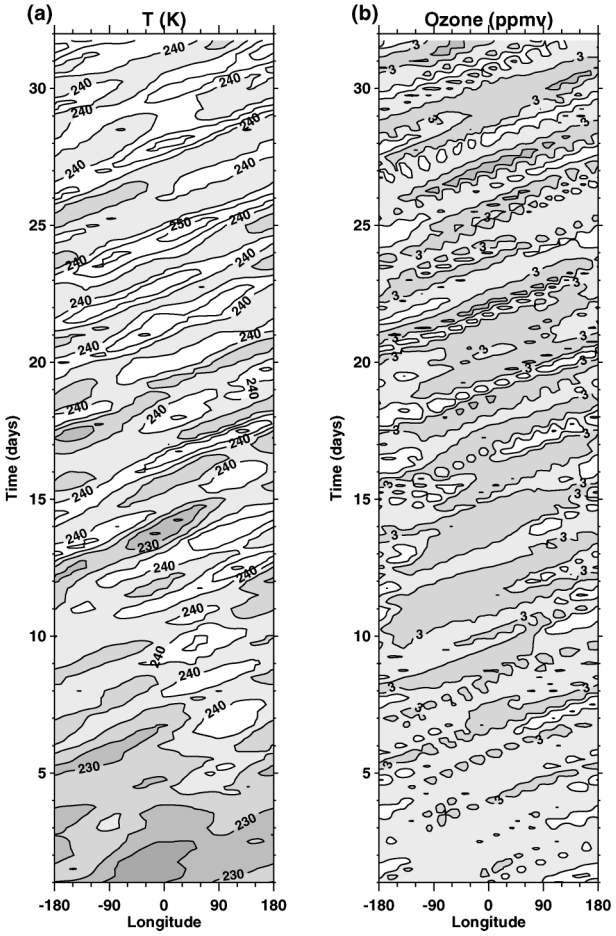

FIG. 1. Longitude–time plot of (a) temperature (K) and (b) ozone mixing ratio (ppmv) at 70°S and 2 hPa for Jul 1998. Temperature contour interval is 5 K. Cooler temperatures are shaded. Ozone contour interval is 1 ppmv. Lower ozone values are shaded.

temperatures between the two analyses that reflect the difficulties still associated with temperature analyses near the stratopause. The Ertel PV field (Fig. 2b) shows a strong gradient associated with the main polar vortex and a weaker inner vortex associated with the wavenumber-2 feature. Ozone (Fig. 2c) also shows an elongated wave-2 low-ozone region near the pole. The phase of the ozone wave disturbance is somewhat east of the temperature and PV waves. In addition, the zonal wind component (Fig. 2d) shows a wave-2-shaped region of weak winds over the Pole. The zonal wind is of interest because its meridional derivative can help to create the negative regions of potential vorticity gradient q_y needed for instability of the zonal flow. Negative regions of quasigeostrophic potential vorticity gradient are shaded in Fig. 2d. The three negative regions associated with the inner vortex change with time as the fast inner vortex interacts with the slower changing main vortex. Though this paper focuses on the waves interacting with a zonally averaged basic state, the complicated negative q_y pattern, with its lack of zonal symmetry, should be kept in mind. In addition to wave 2, the patterns in Fig. 2 show a wave-1 component as well, in that the disturbance is centered somewhat off the Pole; however, the wave-2 feature stands out more clearly at this time.

A representative 6-month time series (April–September 1998) of temperature and ozone at a point at 70°S and 2 hPa (Fig. 3) shows 2–4-day fluctuations throughout the time period. The temperature and ozone oscillations increase in amplitude during July 1998, though the ozone shows larger-amplitude disturbances than temperature in May and June. There is some evidence here (verified by spectral analysis) that the period of the oscillations is higher in July than in August. This corresponds to dominance of wave 2 over wave 1 in July shown below.

Figure 4 shows the zonally averaged temperature and ozone at 2 hPa as a function of time and latitude. While the ozone gradients increase somewhat with time, the temperature structure changes dramatically in July 1998, with a relatively warm region forming at 60°–70°S and increased meridional temperature gradients poleward of 70°S. These temperature changes are related to the seasonal downward motion of the wintertime jet and formation of a double jet near the stratopause. As will be shown, this warm region is where the wave-2 component of the 4-day wave is found.

The following figures highlight the month of July 1998 because spectral analysis of the months May–September 1998 (not shown) revealed that the wavenumber-2 component was much larger than the wavenumber-1 component during July.

Figure 5a shows the zonal mean zonal wind for the month of July 1998 and its associated negative region of $\overline{q}_y$. The jet tilts strongly equatorward with altitude with a weak poleward secondary maximum at the uppermost levels. In between the two jets is the negative $\overline{q}_y$ region. The critical line for the 0.58 day^{-1} wave (described in more detail below) and the $\overline{q}_y = 0$ line coincide at upper levels, in the region between the two jets. The reference level at 0.4 hPa shows how there can be three critical levels at a given altitude. Figure 5b shows the zonal mean temperatures for July 1998. The dashed line shows where the meridional temperature gradient is zero. A region of reversed temperature gradient (warm air toward the pole) extends from the mesosphere down into the stratosphere. As will be shown, this region is where the temperature perturbation wave-2 component of the 4-day wave has a maximum. The possible significance of this reversed temperature gradient region is discussed in section 6.

Figure 6 shows the July 1998 eastward-propagating temperature and ozone frequency spectrum as a function of pressure at 70°S for wave 1 and wave 2. Also plotted is the critical line, derived from the zonal mean zonal wind, for each frequency and wavenumber. Note that most wave activity is bounded by the critical line indicating that the waves are regressing with respect to the zonal mean winds as expected for Rossby waves.

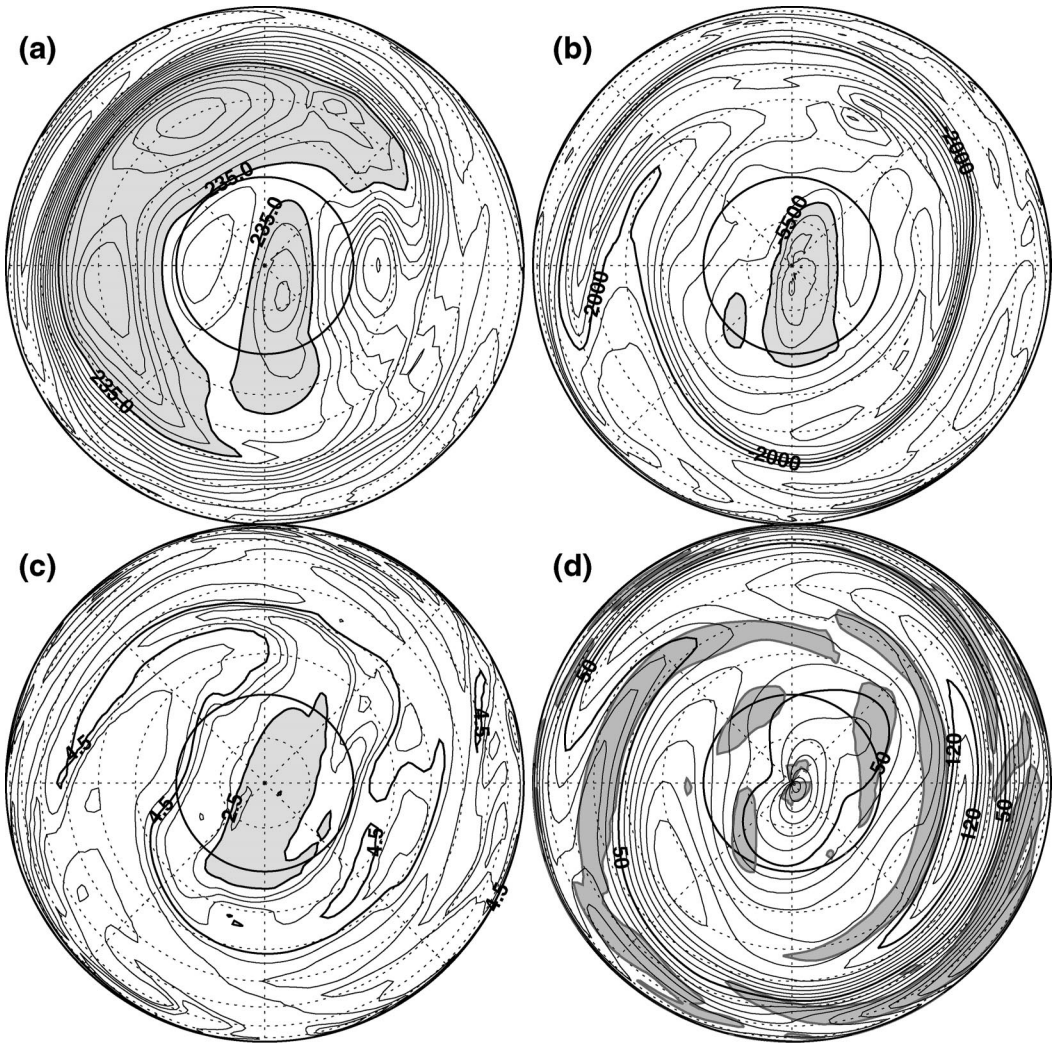

FIG. 2. Circulation at 2 hPa at 1200 UTC 16 Jul 1998: (a) temperature (K), temperatures less than 235 K shaded, contour interval 2.5 K; (b) potential vorticity (PVU, where 1 PVU = 1×10^{-6} K m^2 kg^{-1} s^{-1}), PV less than -5500 PVU shaded, contour interval 500 PVU; (c) ozone (ppmv), ozone less than 2.5 ppmv shaded, contour interval 0.5 ppmv; and (d) zonal wind component (m s^{-1}), q_y less than zero is shaded, contour interval 10 m s^{-1}. Orthographic projection from the equator to the South Pole, 90°E at the bottom of the plots, highlighted latitude at 70°S.

The wave-1 temperature spectra (Fig. 6a) are large for the stationary and slowly propagating waves; however the amplitudes are relatively weak and poorly defined near the 4-day wave frequency (0.25 day^{-1}). The wave-1 ozone spectra (Fig. 6b) show a stationary wave peak at 2 hPa and a weak ozone peak at a fairly high period (0.4 day^{-1}) very near the critical line. The wave-2 temperature spectra (Fig. 6c) show a large, vertically coherent peak at about 0.6 day^{-1}. This is the wave-2 structure; the period is about 1.7 days. The spectral peak maximizes between 1–2 hPa and extends from the top of the domain down to the critical line. The wave-2 ozone spectra (Fig. 6d) shows a similar 0.6 day^{-1} peak, though it is much more localized in the vertical than the wave-2 temperature peak. Ozone also tends to show a weak peak at higher frequencies near the critical line, similar to the wave-1 ozone spectra.

The same frequencies as a function of latitude, at 2 hPa, are shown in Fig. 7. Once again the waves are generally constrained by the critical line to be propagating more slowly than the zonal mean flow. An exception seen here is near the equator where the peaks in the temperature spectra are likely to be Kelvin waves. The wave-1 temperature spectra (Fig. 7a) show the largest amplitudes at low frequencies (periods greater than 10 days). Poleward of 70°S, there is a weak peak at 0.25 day^{-1}. The wave-1 ozone spectra (Fig. 7b) show low-frequency waves along with high-frequency peaks poleward of 70°S. As in Fig. 6, the ozone tends to show peaks near the critical line and some weak peaks at even higher

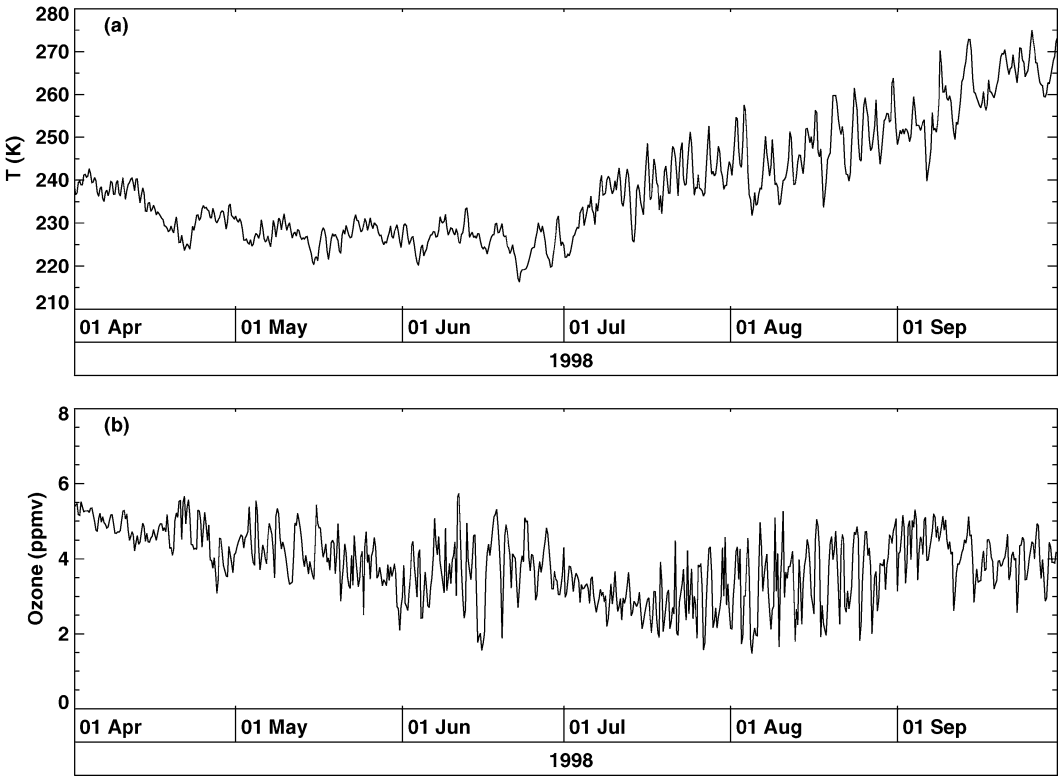

FIG. 3. Time series of (a) temperature (K) and (b) ozone (ppmv) at 70°S, 0°. Time resolution is 6 h. Altitude is 2 hPa.

frequencies than the critical-level frequency. The wave-2 temperature spectra (Fig. 7c) show low-frequency waves equatorward of 60°S and the high frequency peak, as before, at 0.6 day^{-1}. The wave-2 ozone spectra (Fig. 7d) also show the 0.6 day^{-1} peak, along with peaks at higher frequencies near the critical line. The tendency seen here for the ozone frequencies to peak near the critical line may represent advection of ozone features by the zonal mean wind and is discussed further in section 5. Figure 7 shows that the high-frequency wave is larger and more well defined in wave 2 than wave 1 during July 1998, in agreement with Fig. 6.

As pointed out by Allen et al. (1997) and others, the 4-day wave structure is determined by hydrostatic and quasigeostrophic balance relations. The wave structure around a latitude circle can be considered as a series of high and low geopotential height perturbations. For example, in a low geopotential height region, hydrostatic balance dictates that the temperature is cold below and warm above. Thus, a vertical temperature dipole is expected for the wave, with out-of-phase temperature perturbations above and below the region of the geopotential height perturbation. For winds, quasigeostropic balance requires a cyclonic circulation around a low geopotential height perturbation, implying that winds peak in amplitude at the same level as the pressure perturbation but with different horizontal structure. The meridional wind amplitude will peak at the same latitude as the height perturbation; however, it will be a quarter wavelength out of phase in longitude compared to the height perturbation. The zonal wind amplitude will consist of two out-of-phase peaks in latitude forming a dipole about the geopotential height perturbation amplitude peak. According to quasigeostropic theory, potential vorticity perturbations in the Southern Hemisphere should be well correlated with geopotential height perturbations. These relations are illustrated in Allen et al. (1997, see their Fig. 14a). In this study, only the lower peak of the temperature dipole can been seen, because the DAO pressure level output stops at 0.2 hPa. However, the geopotential height wave can be examined near its peak, at an altitude above the lower temperature peak.

Figure 8 shows the wave-1 and wave-2 geopotential height spectra for July 1998 at 0.4 hPa as a function of latitude. The PV spectra were very similar to the geopotential height spectra and are not shown here. The wave-1 spectra (Fig. 8a) show the largest peaks for the low-frequency waves with smaller peaks poleward of 70°S at 0.25 day^{-1} and higher frequencies. The wave-2 spectra (Fig. 8b) show some low-frequency waves equatorward of 60°S and a well-defined high-frequency peak at 0.6 day^{-1}. This high-frequency wave-2 peak occurs near the intersection of the critical line and the latitude where $\overline{q}_y = 0$, in agreement with expectations from the linear theory of barotropically growing waves (as discussed in Hartmann 1983). Because of the double-

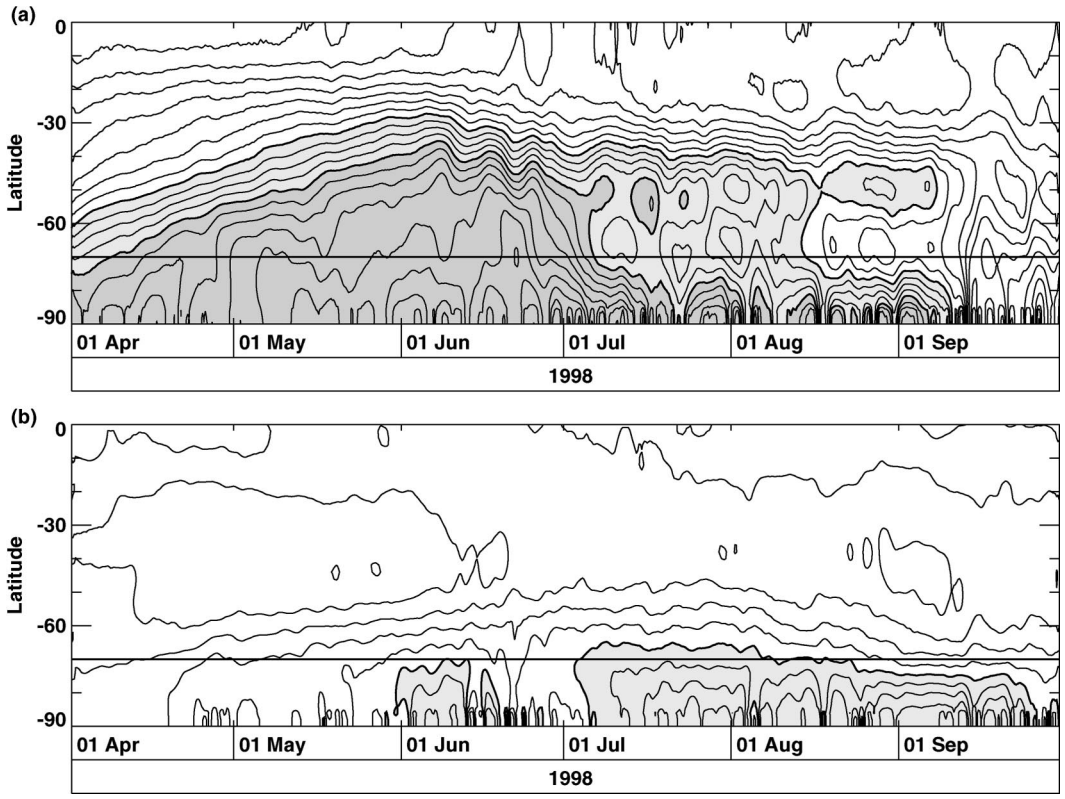

FIG. 4. Latitude–time contour plot of (a) temperature (K), 5-K contour interval, dark shading is temperature less than 235 K, light shading is temperature less than 245 K; and (b) ozone (ppmv), 1-ppmv contour interval, shading is ozone less than 3.5 ppmv. Altitude is 2 hPa. Horizontal line is at 70°S.

peaked jet at these altitudes, the wave-2 frequencies from 0.55–0.6 day^{-1} have three critical lines (as can be seen in Fig. 8), and the two most poleward critical lines are close to the two $\overline{q}_y = 0$ lines that bound the negative $\overline{q}_y$ region between the two jets. Thus, the monthly averaged zonal mean zonal wind in July 1998 provides ample opportunity for the development of wave-2, 0.55–0.6 day^{-1} modes. What is not clear is why wave 2 is singled out for development rather than the corresponding wave-1 frequencies, although the instability studies reviewed in section 1 suggest that the wavenumber of the most unstable wave is sensitive to the horizontal and vertical curvature of the zonal wind.

The next two plots (Figs. 9 and 10) present a series of latitude–pressure sections of the July 1998 wave-2 structure at a single frequency, 0.58 day^{-1} (1.72-day

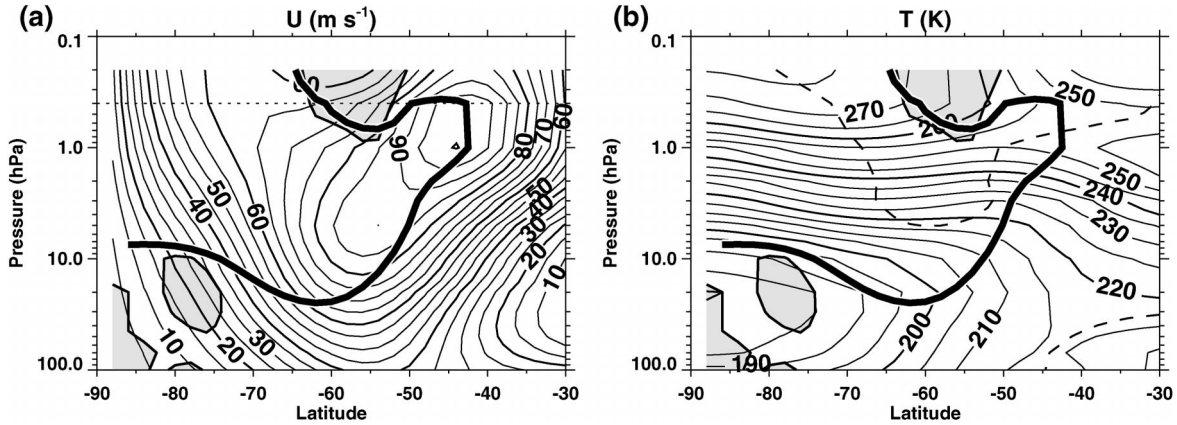

FIG. 5. Zonal mean structure for Jul 1998: (a) zonal mean zonal wind (m s^{-1}) with dotted reference line at 0.4 hPa, and (b) zonal mean temperature (K). Thicker-dashed curve is where the horizontal temperature gradient is zero. In both (a) and (b), the shaded region is where $\overline{q}_y$ is negative. The heavy dark curve is the critical line for a 1.72-day period wave-2 disturbance.

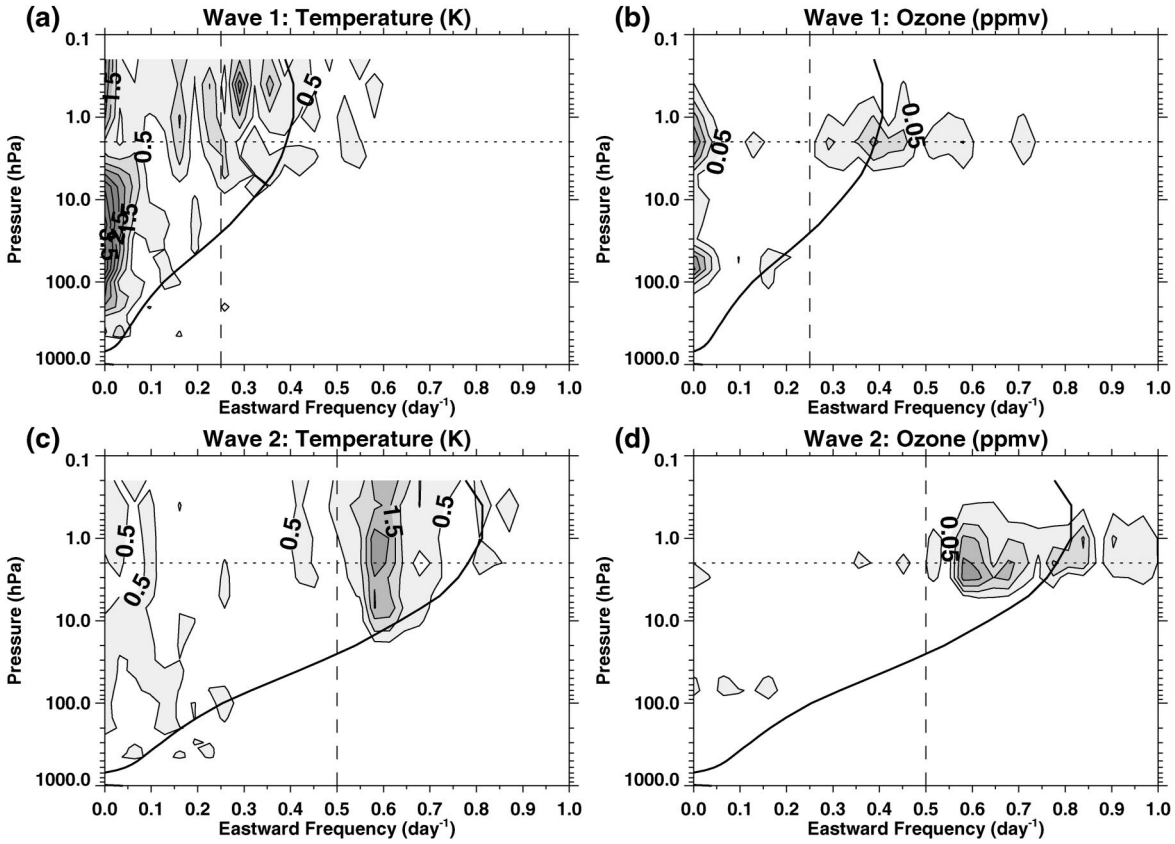

FIG. 6. Jul 1998 wave amplitudes as a function of frequency (day^{-1}) and pressure at 70°S: (a) wave-1 temperature (K), (b) wave-1 ozone (ppmv), (c) wave-2 temperature (K), and (d) wave-2 ozone (ppmv). Temperature contour interval 0.5 K. Ozone contour interval 0.05 ppmv. The thicker solid-curve plots the critical line at 70°S. The vertical dashed lines highlight the 4-day (for wave 1) and 2-day (for wave 2) frequencies. The horizontal dotted line is at 2 hPa. Values below 500 hPa are not shown. Larger amplitudes are shaded.

period), that corresponds to the main wave-2 peak seen in the spectra. The critical line for this frequency is repeated on all the plots as a reference curve. Note that these plots are more limited in altitude (100–0.2 hPa) and latitude (90°–30°S) than previous plots to better focus on the region of interest.

Figure 9a shows the wave-2 temperature amplitude and phase. As mentioned above, only the lower lobe of the temperature structure is seen at these altitudes, though the phase is changing rapidly with height at the top level, as expected, and there is some hint of an increase in amplitude beginning at 0.2 hPa. The temperature wave maximum (about 2.5 K) occurs right where the mean temperature gradients are reversed (Fig. 5b). The ozone amplitude maximum (Fig. 9b) is more poleward and lower down than the corresponding maximum in temperature amplitude. The ozone amplitude (maximum about 0.2 ppmv) is more confined in the vertical than the temperature amplitude and the ozone phase emphasizes the change in phase with latitude.

Figure 9c shows the wave-2 geopotential height field for July 1998. The maximum height amplitude (about 80 m) is near the critical line. Note that the phase contour interval has been increased when compared to the temperature and ozone phase plot (Figs. 9a,b). The phase of the geopotential height varies little in the maximum amplitude region. The phase structure will be discussed more below.

Figure 9d superimposes the ozone amplitude on top of a plot of the meridional gradient of the zonal mean ozone. The ozone wave amplitude peaks where the geopotential height amplitude (Fig. 9c) overlaps the peak in horizontal ozone gradient. The amplitude of the meridional wind perturbation associated with the wave (not shown) is well correlated with the amplitude of the geopotential perturbation (through geostrophic balance); this implies that horizontal advection by the wave acting in a region of strong latitudinal ozone gradients is one component responsible for the ozone wave signal, in agreement with the findings of Manney et al. (1998). Vertical advection is probably much less important as ozone vertical gradients become zero at the peak of the ozone mixing ratio. Temperature-dependent ozone chemistry will begin to have an effect in the upper stratosphere and some departure of the ozone signal from pure advection can be expected at 2 hPa (Allen et al. 1997). For the case in Allen et al. (1997), where ozone loss is proportional to the temperature pertur-

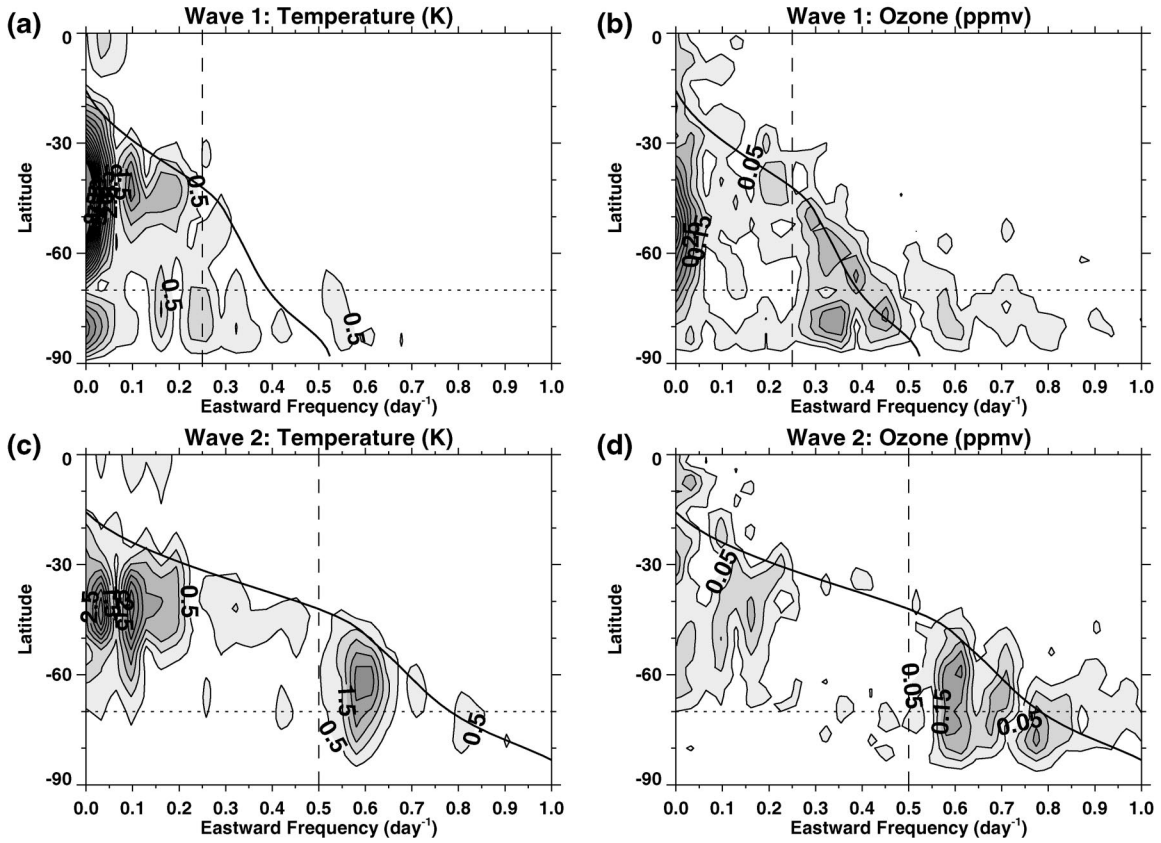

FIG. 7. Jul 1998 wave amplitudes as a function of frequency (day^{-1}) and latitude at 2 hPa: (a) wave-1 temperature (K), (b) wave-1 ozone (ppmv), (c) wave-2 temperature (K), and (d) wave-2 ozone (ppmv). Temperature contour interval is 0.5 K. Ozone contour interval is 0.05 ppmv. The thicker solid-curve plots the critical line at 2 hPa. The vertical dashed lines highlight the 4-day (for wave 1) and 2-day (for wave 2) frequencies. The horizontal dotted line is at 70°S. Larger amplitudes are shaded.

bation, air flowing eastward through the warm temperature region would lose ozone, implying a tendency toward a quadrature relation between ozone and temperature. In Fig. 2, ozone appears to be mainly in phase with the temperature in the polar regions, as expected from horizontal advection, though the ozone pattern is shifted somewhat to the east of the temperature pattern at this time, perhaps a result of temperature-dependent ozone photochemistry.

Figure 10a plots the EP flux divergence and the EP flux vectors calculated from the assimilated winds and temperatures for the July 1998 wave-2 height field. The divergence is centered at about 1 hPa and 58°S with extensions up into the negative $\overline{q}_y$ region and across over a broad latitude range (70°–50°S) at 2 hPa. The EP flux vectors point into three convergence regions: equatorward (and above), poleward (and above), and below the divergence region. Linear instability theory predicts growing waves consist of a dipole of EP flux divergence and convergence with the EP flux vectors pointing across the $\overline{q}_y = 0$ line [consistent with a zero right-hand side in Eq. (2)] from divergence to convergence. [See Hartmann (1983) for a discussion of the barotropic problem and Manney and Randel (1993) for baroclinic examples.] While there is some overlap of the EP flux divergence region in Fig. 10a with the negative $\overline{q}_y$ region (Fig. 5a), most of the divergence is in the positive $\overline{q}_y$ region. However, since this is a time-averaged plot, the linear growing wave model may not be expected to apply and the time-averaged versions (with the time rate of change terms set to zero) of Eqs. (1) and (2) may provide a more appropiate interpretation. In this case the divergent region would be balanced by dissipation and nonlinear effects.

The July 1998 wave-2 EP flux vectors (Fig. 10a) show a more complex case than what is usually modeled. The poleward and equatorward EP flux vectors show that both poleward and equatorward momentum fluxes are associated with the wave. This helps explain the geopotential height field phase variations shown in Fig. 9a at upper levels where the meridional phase gradient changes sign. Downward EP flux vectors have been reported by Randel and Lait (1991) and Allen et al. (1997) and in the linear instability model of Manney and Randel (1993). These downward EP flux vectors are not surprising in a middle atmosphere instability event; however, they contrast with the usually upward direction associated with planetary waves propagating upward

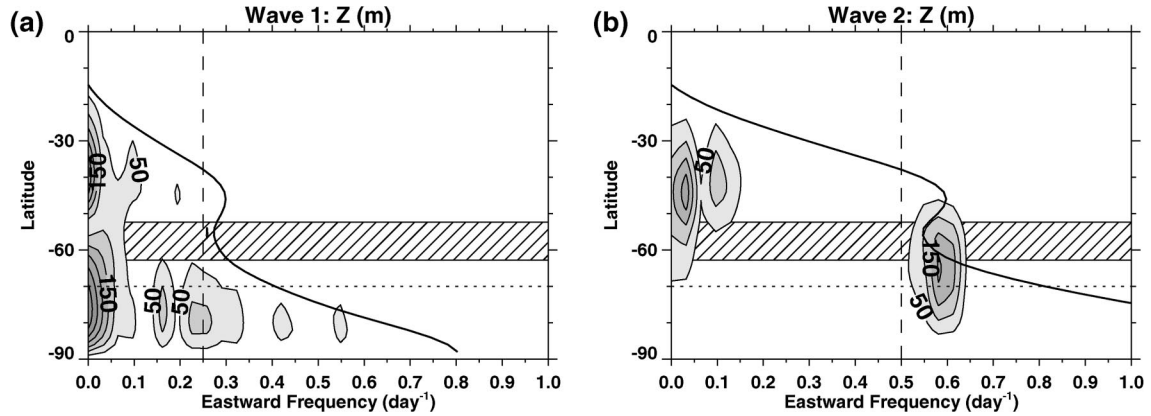

FIG. 8. Jul 1998 geopotential height amplitudes (m) as a function of frequency (day^{-1}) and latitude at 0.4 hPa: (a) wave 1 and (b) wave 2. Contour interval 50 m. The thicker solid curve plots the critical line at 0.4 hPa. The diagonally striped region denotes latitudes where $\overline{q}_y$ is negative. The vertical dashed lines highlight the 4-day (for wave 1) and 2-day (for wave 2) frequencies. The horizontal dotted line is at 70°S. Larger amplitudes are shaded.

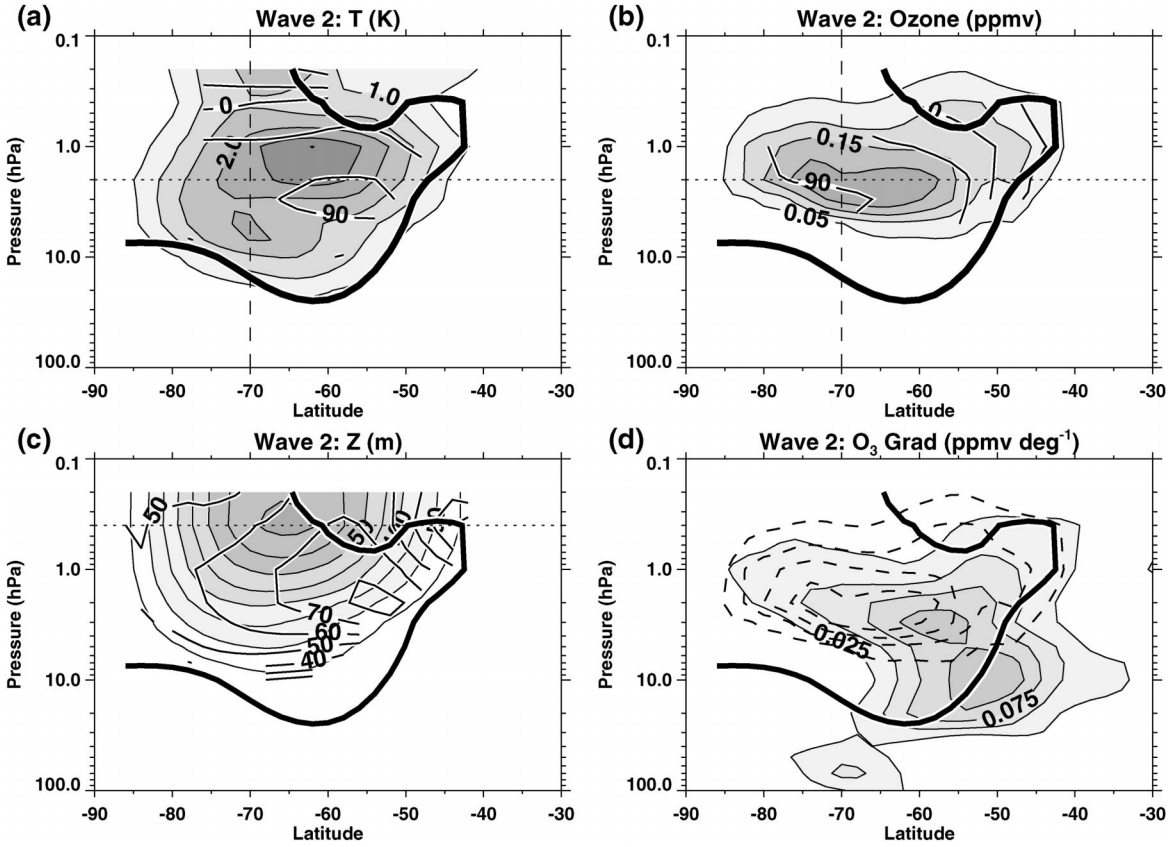

FIG. 9. Wave-2 structure, Jul 1998, 1.72-day period, as a function of latitude and pressure. The heavy dark curve is the critical line. (a) Temperature wave amplitude (K, shaded contours, contour interval 0.5 K) and phase (degrees, black lines, contour interval 45°). (b) Ozone wave amplitude (ppmv, shaded contours, contour interval 0.05 ppmv) and phase (degrees, black lines, contour interval 45°). Reference broken lines at 70°S and 2 hPa are shown in (a) and (b). (c) Geopotential height wave amplitude (m, shaded contours, contour interval 10 m, maximum contour is 80 m) and phase (degrees, black lines, contour interval 10°) with dotted reference line at 0.4 hPa; (d) mean latitudinal ozone gradient (ppmv deg^{-1}, shaded contours, contour interval 0.025 ppmv deg^{-1}) and ozone wave amplitude (dashed lines) repeated from (b).

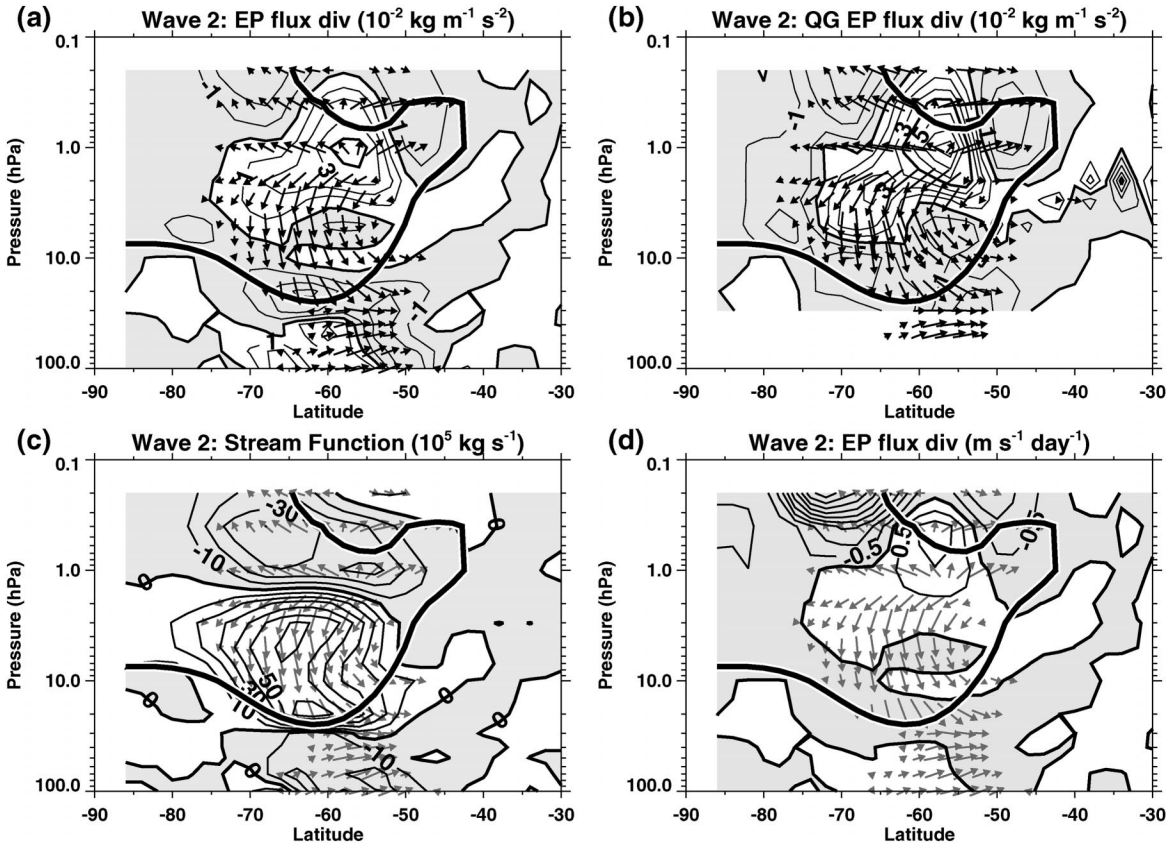

FIG. 10. Wave-2 structure, Jul 1998, 1.72-day period, as a function of latitude and pressure. The heavy dark curve is the critical line. (a) EP flux divergence (10^{-2} kg m^{-1} s^{-2}), negative values are shaded, contour interval 10^{-2} kg m^{-1} s^{-2}, and arrows depict the EP flux vectors. (b) Same as (a), except calculated from heights using quasigeostrophic approximation. (c) Wave-induced mass streamfunction (10^5 kg s^{-1}, negative values are shaded, contour interval 10×10^5 kg s^{-1}) and EP flux vectors from (a). (d) Zonal mean wind forcing (m s^{-1} day^{-1}, negative values are shaded, contour interval 0.5 m s^{-1} day^{-1}) and EP flux vectors from (a).

from the troposphere. The net EP flux is still upward at this time, as the forced upward planetary fluxes are much larger than the fluxes associated with the local instability. These downward EP flux vectors penetrate to below 10 hPa where they abate in a region of EP flux convergence near the lower part of the critical line.

Figure 10b shows the same fields as in Fig. 10a, but they are calculated using only the assimilated geopotential height field amplitude and phase shown in Fig. 9c, using the quasigeostrophic approximation. Though the magnitudes are larger, the quasigeostrophic approximation shows remarkable agreement with the full calculation. This lends support to observational EP flux studies based only on satellite-derived height fields and also supports the use of Eq. (2) in the interpretation of the complete (nonquasigeostrophic) EP flux divergence shown in this study.

Figure 10c plots the heat-flux-based mass streamfunction (meridional heat flux divided by the mean stability) associated with the 0.58 day^{-1} wave 2. This shows the wave's contribution to the residual streamfunction (see Holton 1992, p. 324, for a definition of the residual streamfunction). The circulation is equatorward at 2 hPa, opposite the poleward motion forced by upward-propagating planetary waves. The total circulation will be dominated by the upward-propagating planetary waves; however, the higher-frequency wave contribution to the total residual streamfunction can be seen as a perturbation in the overall downward poleward motion (not shown).

The EP flux divergence is replotted (Fig. 10d) with a density scaling to better quantify the induced mean wind tendency. Most of the tendency occurs at the lowest density level shown, with the EP flux divergence acting to accelerate the wind in the region between the two jets and with the EP flux convergence acting to decelerate the jet winds, especially the poleward jet. The maximum deceleration shown is about 4 m s^{-1} day^{-1}.

The time behavior during July 1998 is examined by first putting the assimilation fields through a simple bandpass filter that retains only eastward-propagating wave-2 frequencies between 0.4–1.0 day^{-1} (1.0–2.5-day periods). Figure 11 (left) shows the EP flux divergence at 2 hPa as a function of latitude and time based on the filtered assimilation products. The EP flux divergence shows how the wave forcing of the zonal mean

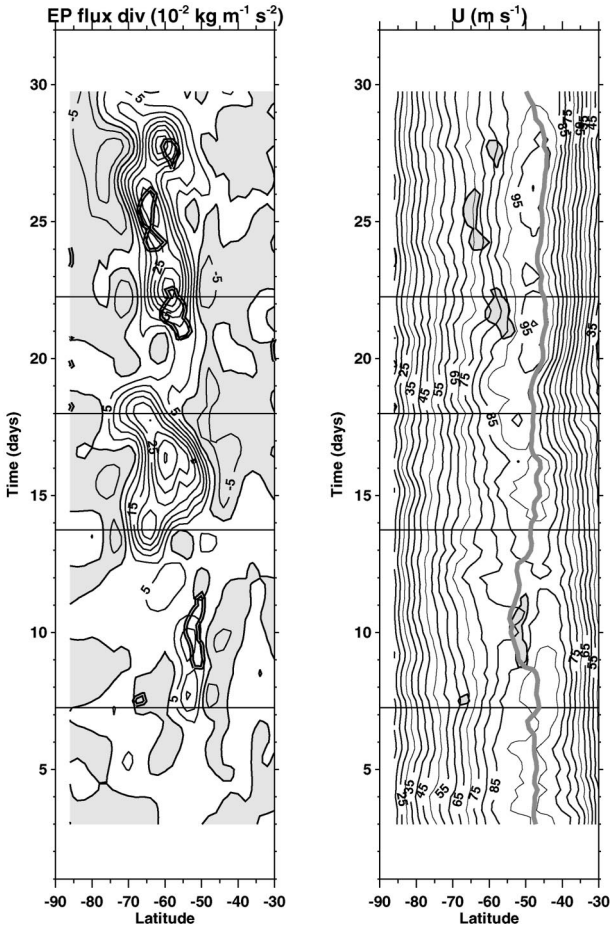

FIG. 11. Time–latitude plots at 2 hPa for Jul 1998: (left) bandpass-filtered EP flux divergence ($\times 10^{-2}$ kg m^{-1} s^{-2}), contour interval 5 $\times$ 10^{-2} kg m^{-1} s^{-2}, negative values shaded, negative $\overline{q}_y$ regions double outlined. (right) Zonal mean zonal wind (m s^{-1}), contour interval 5 m s^{-1}, negative $\overline{q}_y$ regions shaded. Thick gray line is the 0.58 day^{-1} critical line. The four horizontal lines correspond to the four times shown in Fig. 13.

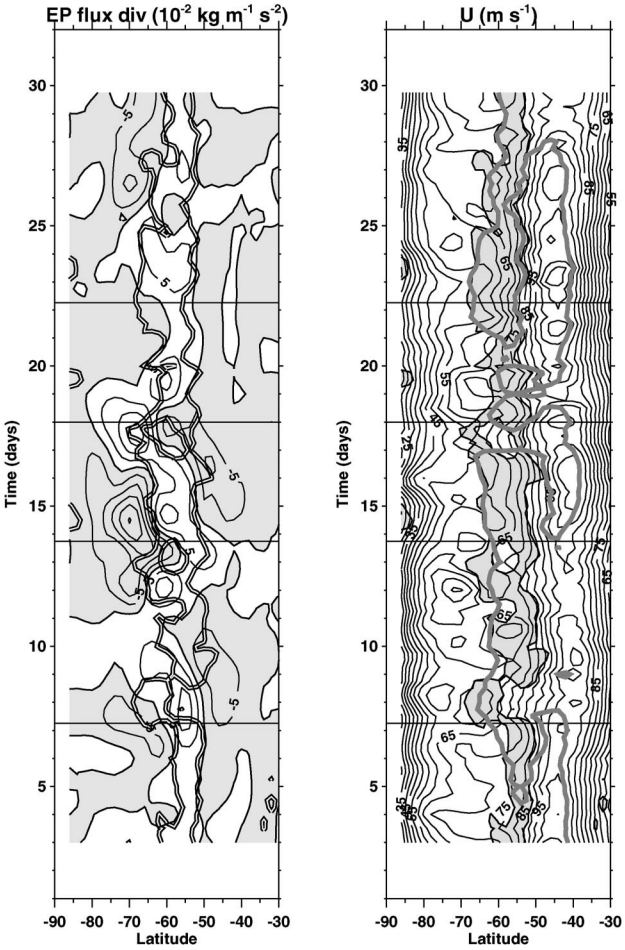

FIG. 12. As in Fig. 11, but for the 0.4-hPa level.

zonal wind changes over the course of the month. The peak EP flux divergence location varies from ~55°S early in the month to ~60°–70°S later in the month. The largest values of EP flux divergence start on 13 July 1998 and consist of six peak events (13, 16, 18, 22, 25, and 28 July). Figure 11 (right) shows the time evolution of the zonal mean zonal wind along with the 0.58 day^{-1} critical line and the negative $\overline{q}_y$ regions, all at 2 hPa. The three later EP flux divergence peaks (22, 25, and 28 July) are seen to occur about a half a day after the center of corresponding negative $\overline{q}_y$ regions. There is also some overlap between the EP flux divergence on 9 July and a negative $\overline{q}_y$ region.

Figure 12 shows the same fields as Fig. 11 at 0.4 hPa. The zonal mean zonal wind (Fig. 12, right) shows the double jet structure at these altitudes with a persistent region of negative $\overline{q}_y$ located between the two jets. Unlike the nearly constant single critical line at 2 hPa, at 0.4 hPa there are often times when the 0.58 day^{-1} critical line is found at three latitudes. Note how the 0.58 day^{-1} critical line mirrors the most poleward $\overline{q}_y = 0$ line during most of the time shown and tracks closely the middle critical line about half of the time shown. The EP flux divergence at 0.4 hPa is mainly in the negative $\overline{q}_y$ region with EP flux convergence outside the negative $\overline{q}_y$ region as expected from linear stability arguments for growing waves. This relation is especially apparent on 14 July.

Figure 13 shows the EP flux divergence and the zonal mean zonal wind at four times: 0600 UTC 7 July, 1800 UTC 13 July, 0000 UTC 18 July, and 0600 UTC 22 July. Because these fields are not time averages and contain a range of frequencies, the magnitude of the EP flux vectors and their divergences are larger than in the monthly averaged, single-frequency plots previously shown in Fig. 10 and the vectors and contours have been rescaled for these plots.

Early in the month (Fig. 13a), the EP flux divergence is relatively weak and located at a relatively low latitude (55°S). There are two EP flux convergence regions both poleward and equatorward of the peak divergence region, with EP flux vectors pointing from the divergence

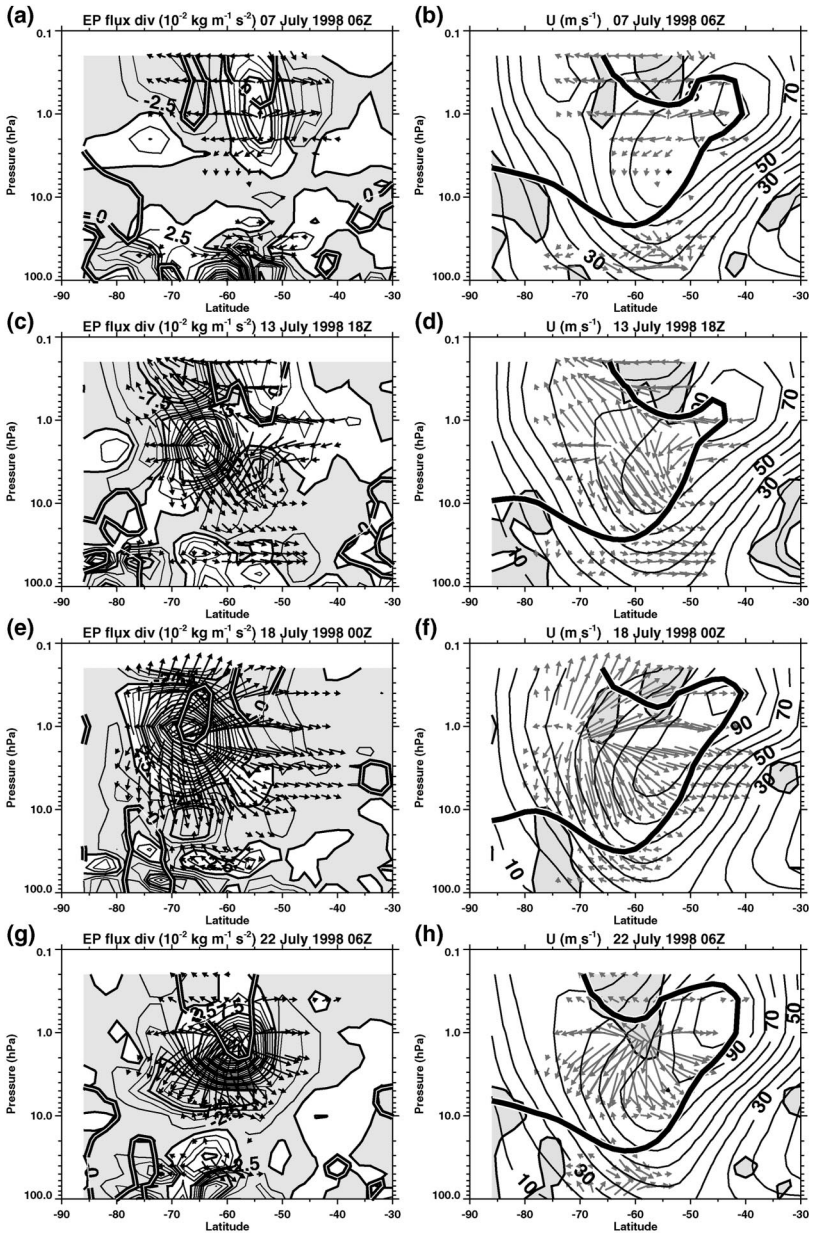

FIG. 13. Plots of (a), (c), (e), (g) EP flux divergence (contour interval 2.5 $\times$ 10^{-2} kg m^{-1} s^{-2}, negative values are shaded) and (b), (d), (f), (h) zonal mean zonal wind (contour interval 10 m s^{-1}) at four times during Jul 1998. Eliassen–Palm flux vectors are scaled to be 40% smaller than in Fig. 10 to aid readability. The heavy line on the right is the critical line for a 1.72-day period wave-2 mode. Negative $\overline{q}_y$ regions are shaded on the right, and $\overline{q}_y = 0$ are double lines on the left.

region into the convergence regions. These vectors correspond to both equatorward and poleward momentum fluxes at this time. This pattern of EP flux divergence will tend to accelerate the winds between the split jet (Fig. 13b) and decelerate both jets, reducing the amplitude of the negative $\overline{q}_y$ region as expected for unstable waves. The EP flux divergence at this time is somewhat correlated with the negative $\overline{q}_y$ region located between the split jet.

By 13 July, the EP flux divergence (Fig. 13c) is much stronger and the peaks are displaced farther poleward (65°S). While the EP flux divergence peaks below the negative $\overline{q}_y$ region, there is still an EP flux divergence region above 1 hPa that is well correlated with the negative $\overline{q}_y$ region. There are two EP flux convergence regions at this time: one above and poleward of the main divergence peak, and one below the EP flux divergence region. The EP flux vectors are mainly poleward at this

time (equatorward momentum fluxes) except down near 10 hPa where the EP flux vectors head toward the critical line (Fig. 13d).

An even more poleward EP flux divergence peak is found on 18 July (Fig. 13e), and it is clearly associated with a high-latitude negative $\overline{q}_y$ region. The poleward jet is very weak at this time (Fig. 13f) and most of the EP flux vectors equatorward of 70°S point equatorward (poleward momentum flux). The EP flux convergence region completely encircles the divergence region with especially strong convergence above and below the divergence region.

Just 4 days later (about one rotational period) the EP flux divergence peak (Fig. 13g) is more equatorward (58°S), and there are large regions of both poleward and equatorward EP flux vectors. The EP flux divergence is well correlated with a negative $\overline{q}_y$ region, and the double jet structure has returned (Fig. 13h). The EP flux convergence region wraps almost completely around the divergence region.

These plots show that the positions of the EP flux divergence and negative $\overline{q}_y$ regions vary over the course of the month. In general the strong EP flux divergence regions are closely associated with a negative $\overline{q}_y$ region; however, the EP flux divergence regions are often strong outside the negative $\overline{q}_y$ region. Thus the complete correlation between the two fields expected from linear theory for growing waves [as discussed with Eq. (2)] does not occur, implying that the waves are either decaying or influence by frictional, diabatic, nonlinear, or ageostrophic effects in some regions.

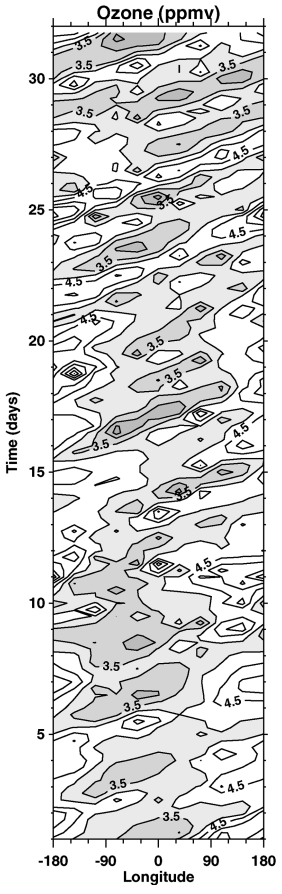

FIG. 14. Longitude–time plot of POAM ozone (ppmv) at an average latitude of 68°S and 2 hPa for Jul 1998. Contour interval is 0.5 ppmv. Lower ozone values are shaded.

4. POAM ozone data

This section presents the Polar Ozone and Aerosol Measurement (POAM) ozone data (Lucke et al. 1999) that observationally validates key features of the 4-day wave as seen in the DAO ozone assimilation. During July 1998 the POAM ozone observations were confined between about 65°–70°S and therefore will be treated as being at a constant latitude. There are ~14 ozone profiles taken each day. This does not give much resolution for a longitude time plot; nevertheless, Fig. 14 shows one attempt to interpolate the longitude–time POAM observations at 2 hPa to a regular grid suitable for contouring the high-frequency waves. Comparing with the assimilation ozone (Fig. 1b), the POAM observations show a similar time mean wave-1 structure and propagating wave-2 feature. The amplitude of the wave-2 signal in the POAM ozone is nearly the same as in the DAO ozone assimilation (the contour interval is doubled in Fig. 14), although there is an offset to slightly higher overall values of ozone in the POAM observations. Note that lower resolution, combined with interpolation, results in smoother contours in the POAM longitude–time figure than in the corresponding DAO ozone figure.

Figure 15 provides more quantitative evidence of the high-frequency wave in the POAM observations using an analysis method similar to that of Prata (1984). Here, the POAM observations at each level are taken as a time series for the month and a Fourier transform is performed on the month-long time series (431 points at each level for the month of July 1998). This method does not separate out the wavenumber dependence; however, stationary waves 1 and 2 would correspond to 1 and 2 day^{-1} frequencies, respectively (as the earth rotates under the satellite), and 4-day rotational period; eastward-propagating waves 1 and 2 would correspond to 1.25 and 2.5 day^{-1} frequencies, respectively (by adding the frequency of the wave motion to the corresponding frequency associated with the earth's rotation). The results are plotted in two frequency ranges (Figs. 15a and 15b) to aid in making comparisons with Figs. 6b and 6d. Figures 15a and 15b can be interpreted as wave-1 and wave-2 plots, though this interpretation of the POAM observations is not unique.

Spectral analysis of the POAM time series reveals an oscillation near 2 hPa with a frequency of 2.58 days^{-1} (Fig. 15b). A stationary wave 2 would yield a peak of 2 days^{-1} and an eastward-propagating wave 2 would

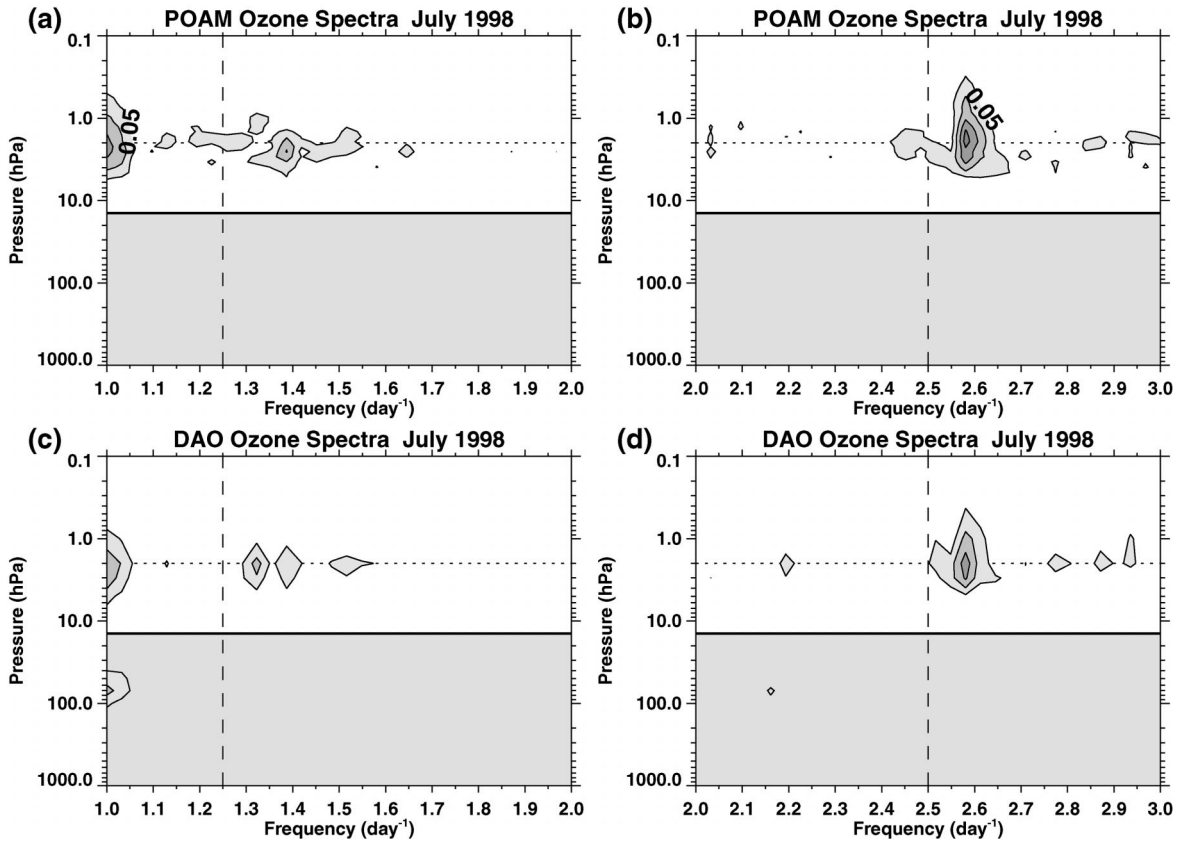

FIG. 15. (a), (b) POAM ozone spectra and (c), (d) DAO ozone spectra (ppmv day) for Jul 1998 as a function of frequency and pressure: (a) and (c) for the frequency range 1–2 day^{-1}; (b) and (d) for the frequency range 2–3 day^{-1}. The contour interval is 0.05 ppmv. Higher values are shaded. The frequency plots are split into two panels to aid in comparison with Figs. 6b and 6d, and corresponding reference lines are drawn. Only POAM observations above 14 hPa (heavy solid line) were analyzed.

have 2 days^{-1} added to its frequency, in this case 0.58 days^{-1}, exactly the peak seen in the DAO ozone assimilation and temperature (Fig. 6). Of course, the peak at 2.58 days^{-1} could also be produced by a very rapidly moving eastward wave 1 or a westward-propagating wave 3. However, the wave-2 interpretation seems most likely in this case, given the DAO assimilation results. Only a portion of the POAM spectrum is shown in Fig. 15; however, the 2.58 day^{-1} frequency peak is the largest spectral peak with the second largest peak being the 1 day^{-1} frequency (stationary wave 1) seen in Fig. 15a. Direct comparisons with the DAO ozone is given in Figs. 15c and 15d, where the DAO ozone assimilation output was sampled at the POAM locations and times. The DAO assimilation ozone shows the same peaks at the same altitudes as the POAM time series, though the amplitudes are somewhat larger in the POAM observations.

Figures 15a and 15b show very small peaks near 1.4 day^{-1} that may correspond to the small wave-1 ozone peak seen in Fig. 6b at 0.4 day^{-1}. As pointed out in the discussion of Fig. 6b, this peak is near the frequency corresponding to the zonal mean wind rotational frequency at that height and latitude.

5. Discussion

The assimilation products shown here display high-frequency planetary-scale waves over the Pole during the Southern Hemisphere winter. Issues to be discussed concern the quality of the assimilation products for high-frequency wave studies, the ability of linear instability theory to explain the results, and the advective peaks seen in the ozone spectra.

a. Quality

The meteorological data going into the fvDAS at these levels (2 hPa) are mainly satellite radiance measurements. That these observations contain the 4-day wave is not surprising given that the early work in studying the 4-day wave (Venne and Stanford 1979, 1982; Prata 1984) was based directly on satellite radiances. The fvDAS used a 1DVAR assimilation (Joiner and Rokke 2000) of satellite radiances and should reflect any waves in these radiances. The ability of the fvGCM (or other GCM) to realistically represent the initiation, propagation, and decay of these waves has not been studied to data. However, the fvGCM has enough res-

olution to assimilate the observations without the loss of information, and the appropriate dynamics and physics to produce the 6-hourly forecasts of the observed wave structure for the next assimilation cycle. The independent POAM observations indicate that the ozone assimilation component, and therefore the advecting winds, are being well handled by the data assimilation system.

The top level of the analysis may be too low to completely characterize the waves. As mentioned in the introduction, the top analysis level is 0.4 hPa with the highest pressure level output being slightly above it at 0.2 hPa. The negative $\overline{q}_y$ region and the wave-2 critical level extend above this altitude. It would be more satisfying if the entire regions of unstable and high zonal wind speeds were captured. The fvGCM does extend to 0.01 hPa so the whole region of instability may indeed be contained by the fvDAS.

The ozone data assimilation system was run without chemistry at this time, relying on observations to correct for photochemical modifications. This may lead to some biases in the mean values and wave amplitudes in the ozone assimilation; however, the basic patterns should be captured via advection by the fvGCM coupled with the ozone observations. Here, the 4-day wave signal in the DAO assimilated ozone agreed well with contemporaneous POAM ozone observations, providing some validation of the O3DAS.

Bandpassed-filtered fields were used here because the 2-day wave signal was well defined and persistent throughout July 1998. Generally the bandpassed-filtered fields closely followed the full wave pattern (by comparison of corresponding maps, not shown); however, there were some specific times (mainly at the end of the month) when the maps based on bandpassed-filtered temperatures did not closely resemble the maps based on the full temperature field. At these times enhanced wave-1 and wave-3 components were also present, and thus, more spectral components or a non-Fourier approach may give further insight into the dynamical situation at these times.

The key to this study was the availability of data assimilation products every 6 h. Such time resolution resolves these fast-propagating and fast-changing waves and thus permits a detailed study of their properties and evolution.

b. Instability theory

This study examined both the monthly averaged and instantaneous EP flux vectors, EP flux divergences, and negative $\overline{q}_y$ regions. The instantaneous fields can be expected to give the best agreement with the developing wave structure predicted by linear instability theory.

In linear instability theory, a negative $\overline{q}_y$ region is correlated with a region of EP flux divergence. Hartmann (1983) found exact correlation in his barotropic model. In their baroclinic model Manney and Randel (1993) also found EP flux divergence and negative $\overline{q}_y$ regions were very closely correlated. In this study, we found that regions of EP flux divergence were not so tightly correlated with negative $\overline{q}_y$ regions. However, the instantaneous EP flux divergences were all closely associated with a negative $\overline{q}_y$ region. Looking at all times during the month (not shown) reveals that the negative $\overline{q}_y$ region often quickly disappears (within 6–12 h) in the vicinity of a growing EP flux divergence. The negative $\overline{q}_y$ region is never completely eliminated, but rather tends to shift to a different latitude or height.

Along with instability, the wave structure seems to show wave propagation away from the source region toward convergence at a critical level. This can be seen in the time-averaged plot (Fig. 10a), where the EP flux vectors converge on the critical line at about 20 hPa. By contrast, EP flux vectors from a linear model shown in Manney and Randel (1993) are only large close to the negative $\overline{q}_y$ region.

Figure 2d shows how zonally asymmetric the negative potential vorticity regions can be. This suggests that (in this example at least) formulating the problem in terms of waves growing on a zonally symmetric unstable state may only be a first step in understanding the origin and evolution of the waves. All of the zonally averaged EP flux divergence regions shown here overlap with negative potential vorticity regions at some longitude (not shown). Additional consideration of the instability of nonzonally symmetric flows (Manney et al. 1989) or a more three-dimensional modeling approach may be needed.

Overall, our study supports earlier linear instability models that associate regions of potential vorticity instability as the source of the waves. The waves propagate (where $\overline{q}_y$ is positive) more slowly than the mean wind in agreement with Rossby wave theory. In addition, the wave's vertical scale decreases as the waves approach the critical line from above, as seen in Fig. 9c where the phase of the geopotential height field begins to change rapidly, again in agreement with linear Rossby wave theory. The frequency of the wave is determined by the frequency of the zonal mean wind rotation around a latitude circle (the heavy line in Fig. 5 is for the 1.72-day period, 0.58 day^{-1} frequency for wavenumber 2) at the $\overline{q}_y = 0$ line in the region between the double jet.

c. Advective ozone peak

While the temperature spectra peak at frequencies that imply phase speeds slower than the zonal mean zonal wind, the ozone spectra show a tendency for additional peaks at frequencies that imply phase speeds that are faster than the zonal mean zonal wind speed (Fig. 7). This may imply that the wave-induced temperature response is more dynamically controlled than the ozone response. Chemistry or diabatic processes may act to create ozone gradients along PV contours allowing the

wave-induced ozone response to have a passive advection signal as well. While no signals like this were seen in the Manney et al. (1998) study of long-lived water vapor and methane, a large fast-moving ozone peak was seen in the spectra presented in Allen et al. (1997). The results here should be interpreted with some caution as these advective peaks were not identified prior to the spectral analysis and may be an artifact of the assimilation process or spectral analysis.

6. Conclusions

This paper has focused on a month (July 1998) when the wave-2 component of the 4-day wave was well defined and persistent. The availability of 6-hourly output from the fvDAS has allowed the first detailed global examination of this fast-moving wave feature. In addition, a companion ozone assimilation allowed identification of the high-frequency wave in the assimilated ozone field.

This wave-2 component (1.7-day period) is generally consistent with past observational studies and linear instability models. Enhanced EP flux divergence is closely associated with negative $\overline{q}_y$ regions with the wave amplitude mainly confined by the critical line to phase speeds westward with respect to the mean flow.

Wave 2 also appears prominently in the DAO ozone assimilation, having an amplitude of about 0.5 ppmv or ~15% of the total ozone mixing ratio at 2 hPa and containing ~50% of the total ozone variance at 70°S. This ozone signal is supported by independent POAM ozone mixing ratio observations. POAM ozone time series at ~70°S shows a spectral peak at 2.58 day^{-1} that is consistent with the assimilation results. The amplitude of the 2.58 day^{-1} signal in POAM (Fig. 14) is very close to the amplitude of the wave 2, 0.58 day^{-1} signal in the DAO ozone assimilation (Figs. 6d and 15d) and both show the ozone spectra at those frequencies peaking near 2 hPa.

The region of reversed temperature gradient was noted in Fig. 5b. This temperature pattern is needed to support the mean wind structure that, in turn, is needed for the 4-day waves to grow. How much, if any, of this mean structure might be caused by the 4-day wave acting on the mean state is still an open question.

The ability of the geopotential height alone to generate the complex EP flux patterns seen in the assimilation-produced wind and temperature fields was illustrated in Figs. 10a and 10b. This implies that, if the geopotential heights are accurate enough, studies of complex EP flux patterns are possible using only geopotential height observations.

While the wave can appear fairly steady over the course of a month, the EP flux divergence pattern can vary significantly over the course of a wave period as shown here for the wave-2 component, and in Randel and Lait (1991) and Lawrence and Randel (1996) for the wave-1 component. This probably indicates that more detailed examination of these waves and their development may be possible using instantaneous PV maps. This leaves open future studies based on assimilation products to further understand the origin and development of high-frequency polar waves.

Acknowledgments. We would like to thank Stephen Eckermann for reviewing an early draft of this work. We would also like to thank the POAM team for guidance in using the POAM ozone measurements. The work was supported in part by the Office of Naval Research. The development and use of the fvDAS was supported by NASA, through their Earth Observation System research program.

REFERENCES

Allen, D. R., J. L. Stanford, L. S. Elson, E. F. Fishbein, L. Froidevaux, and J. W. Waters, 1997: The 4-day wave as observed from the *Upper Atmosphere Research Satellite* Microwave Limb Sounder. *J. Atmos. Sci.,* **54,** 420–434.

Andrews, D. G., J. R. Holton, and C. B. Leovy, 1987: *Middle Atmosphere Dynamics.* Academic Press, 489 pp.

Cohn, S. E., A. DaSilva, J. Guo, M. Sienkiewicz, and D. Lamich, 1998: Assessing the effects of data selection with the DAO physical-space statistical analysis system. *Mon. Wea. Rev.,* **126,** 2913–2926.

Douglass, A. R., M. R. Schoeberl, R. B. Rood, and S. Pawson, 2003: Evaluation of transport in the lower tropical stratosphere in a global chemistry and transport model. *J. Geophys. Res.,* **108,** 4259, doi:10.1029/2002JD002696.

Hartmann, D. L., 1983: Barotropic instability of the polar night jet stream. *J. Atmos. Sci.,* **40,** 817–835.

Holton, J. R., 1992: *An Introduction to Dynamic Meteorology.* Academic Press, 511 pp.

Joiner, J., and L. Rokke, 2000: Variational cloud clearing with TOVS data. *Quart. J. Roy. Meteor. Soc.,* **126,** 725–748.

Kiehl, J. T., J. J. Hack, G. B. Bonan, B. A. Boville, D. L. Williamson, and P. J. Rasch, 1988: The National Center for Atmospheric Research Community Climate Model: CCM3. *J. Climate,* **11,** 1131–1149.

Lait, L. R., and J. L. Stanford, 1988: Fast, long-lived features in the polar stratosphere. *J. Atmos. Sci.,* **45,** 3800–3809.

Lawrence, B. N., and W. J. Randel, 1996: Variability in the mesosphere observed by the *Nimbus 6* PMR. *J. Geophys. Res.,* **101,** 23 475–23 489.

——, G. J. Fraser, R. A. Vincent, and A. Philips, 1995: The 4-day wave in the Antarctic mesosphere. *J. Geophys. Res.,* **100,** 18 899–18 908.

Lin, S. J., 1997: A finite-volume integration method for computing pressure gradient force in general vertical coordinates. *Quart. J. Roy. Meteor. Soc.,* **123,** 1749–1762.

——, and R. B. Rood, 1996: Multidimensional flux-form semi-Lagrangian transport schemes. *Mon. Wea. Rev.,* **124,** 2046–2070.

——, and ——, 1997: An explicit flux-form semi-Lagrangian shallow-water model on the sphere. *Quart. J. Roy. Meteor. Soc.,* **123,** 2477–2498.

Lucke, R. L., and Coauthors, 1999: The Polar Ozone and Aerosol Measurement (POAM) III instrument and early validation results. *J. Geophys. Res.,* **104,** 18 785–18 799.

Manney, G. L., 1991: The stratospheric 4-day wave in NMC data. *J. Atmos. Sci.,* **48,** 1798–1811.

——, and W. J. Randel, 1993: Instability at the winter stratopause: A mechanism for the 4-day wave. *J. Atmos. Sci.,* **50,** 3928–3938.

——, T. R. Nathan, and J. L. Stanford, 1988: Barotropic stability of realistic stratospheric jets. *J. Atmos. Sci.,* **45,** 2545–2555.

——, ——, and ——, 1989: Barotropic instability of basic states with a realistic jet and a wave. *J. Atmos. Sci.*, **46,** 1250–1273.

——, Y. J. Orsolini, H. C. Pumphrey, and A. E. Roche, 1998: The 4-day wave and transport of *UARS* tracers in the austral polar vortex. *J. Atmos. Sci.*, **55,** 3456–3470.

Prata, A. J., 1984: The 4-day wave. *J. Atmos. Sci.*, **41,** 150–155.

Randel, W. J., and L. R. Lait, 1991: Dynamics of the 4-day wave in the Southern Hemisphere polar stratosphere. *J. Atmos. Sci.*, **48,** 2496–2508.

Schoeberl, M. R., A. R. Douglass, Z. X. Zhu, and S. Pawson, 2003: A comparison of the lower stratospheric age spectra derived from a general circulation model and two data assimilation systems. *J. Geophys. Res.*, **108,** 4113, doi:10.1029/2002JD002652.

Štajner, I., L. P. Riishojgaard, and R. B. Rood, 2001: The GEOS ozone data assimilation system: Specification of error statistics. *Quart. J. Roy. Meteor. Soc.*, **127,** 1069–1094.

Venne, D. E., and J. L. Stanford, 1979: Observations of a 4-day temperature wave in the polar winter stratosphere. *J. Atmos. Sci.*, **36,** 2016–2019.

——, and ——, 1982: An observational study of high-latitude stratospheric planetary waves in winter. *J. Atmos. Sci.*, **39,** 1026–1034.